J. Fluid Mech. (2003), *vol.* 493, *pp.* 191–208.
DOI: 10.1017/S0022112003005755 Printed in the United Kingdom

Transverse roll convection in horizontal plane Couette flow

By YUTAKA YOSHIKAWA[1] AND KAZUNORI AKITOMO[2]

[1]Research Institute for Applied Mechanics, Kyushu University, Japan

[2]Graduate School of Science, Kyoto University, Japan

(Received 30 October 2001 and in revised form 24 March 2003)

The structure of thermal convection in horizontal plane Couette flow is investigated. Numerical experiments show that transformation of the structure takes place in the linear stage of perturbation growth. In the non-rotating or slowly rotating case, the transformation from cellular to parallel roll convection occurs. In the rapidly rotating case, on the other hand, the transformation from cellular to parallel roll convection occurs via transverse roll convection. As a result, transverse roll convection of finite amplitude can be formed in the rapidly rotating frame of reference. The formation mechanism of the transverse roll is investigated by linear analysis. In both the non-rotating and rotating cases, the horizontal velocity shear temporarily accelerates the growth rate of the transverse mode for a relatively short period. In the non-rotating or slowly rotating case, however, the net effect of this horizontal velocity shear is small. In the rapidly rotating case, on the other hand, the shearing of the perturbation by the background flow results in greatly enhancing potential energy conversion of the transverse mode. As a result, the net effect becomes large enough to make the transverse mode dominate over the parallel mode. Although the transverse roll convection of finite amplitude appears for a relatively short period of time just after its onset, the present result might explain some aspects of observed transverse rolls, such as in the Jovian atmosphere.

1. Introduction

Thermal convection is one of the fundamental motions of geophysical fluids and plays a central role in transporting heat and material in the vertical direction. As visualized by satellite pictures, the convection is often organized into horizontal rolls (e.g. Kuettner 1959; Miura 1986). Many studies have been devoted to the dynamics of such convection rolls, extensively reviewed by Etling & Brown (1993). Several observational and theoretical studies have found that the velocity shear of the background flow is a possible factor in the organization of a convection roll. For example, linear studies by Kuo (1963) and Asai (1970) showed that with vertical shear of horizontal velocity a convection roll is preferred with its axis parallel to the background flow (parallel roll). Davies-Jones (1971), on the other hand, examined the linear exponential growth of peturbations embedded in a horizontal plane Couette flow in a non-rotating frame of reference, and found that with horizontal velocity shear parallel roll convection is also preferred.

Recently, Yoshikawa, Akitomo & Awaji (2001) performed a numerical experiment on oceanic convection in a baroclinic jet in a rotating frame of reference. Noteworthy is that roll convection with axis obliquely transverse to the background flow (transverse

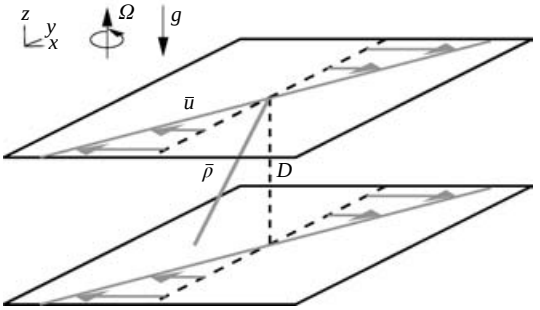

FIGURE 1. Schematic view of the model configuration.

roll) was observed for a short period of time (2–3 days) just after the onset of convection. Although the presence of such a transverse roll in the ocean has not been reported so far (since it is very hard to determine the horizontal structure of oceanic convection on a 1 km horizontal scale), similar transverse rolls have been found in the atmosphere (Miura 1986). They have also been observed around the jet in the Jovian atmosphere. Hathaway & Sommerville (1987) showed that such transverse rolls can be formed by a rotation vector tilted from the vertical direction. However, in the experiment of Yoshikawa *et al.* (2001), the rotation vector is not tilted. Interesting in their experiment is that the orientation of the roll axis changes with time due to shearing of the background flow. This suggests that the horizontal velocity shear organizes convection in the transverse direction, contrary to the results of Davies-Jones (1971).

One factor that is not considered in Davies-Jones (1971) but should be taken into account in explaining observed or simulated transverse rolls is the rotation of the reference frame. Another is the transient nature of the observed phenomena, since the transverse rolls in Yoshikawa *et al.* (2001) are observed over a short period of time. It is known (e.g. Farrell 1993) that the preferred perturbation for a finite period of time is not necessarily the same as that after an infinitely long period of time has passed, the situation examined by Davies-Jones (1971).

The identification of possible factors that characterize convection dynamics is important in understanding the convection in the atmosphere and oceans. The present study is intended to investigate whether the simulated or observed transverse convection rolls are generated by the horizontal velocity shear of the background flow. Numerical experiments are first carried out to examine if with horizontal shear a transverse roll is preferred to a parallel roll, as suggested by Yoshikawa *et al.* (2001), and to explore the conditions for the formation of transverse rolls with particular attention given to the rotation and transient effects. Thereafter, the formation mechanism of transverse rolls is investigated in detail by linear analysis. Finally, there is a discussion of whether or not observed or simulated transverse rolls are explained by the horizontal velocity shear.

2. Model configuration

Convection in an incompressible and Boussinesq fluid with reference density ρ_0, viscosity ν, and diffusivity κ in Cartesian coordinates x, y, z are considered (figure 1). The angular velocity of the rotating reference frame about the vertical axis (z) is Ω. The fluid is bounded by horizontal lids at the top ($z = 0$) and the bottom ($z = -D$).

In order to clearly understand the effects of the horizontal shear of the background flow on convection, we assume a background flow $\overline{u}$ in the x-direction with constant horizontal shear Λ and background fluid density $\overline{\rho}$ with constant vertical stratification Γ:

$$\overline{u} = \overline{u}(y) = \Lambda y, \quad \overline{\rho} = \overline{\rho}(z) = \Gamma z.$$

As in the previous studies, we also assume that the background flow and density are not self-consistently generated but fixed in time by external forcing which remains unspecified (e.g. Davies-Jones 1971). In the rotating reference frame, such a flow can be established by a large-scale pressure gradient balancing the Coriolis acceleration. In a non-rotating reference frame, such a flow can be generated by two non-slip sidewalls moving with different speeds in the x-direction (e.g. Tillmark & Alfredsson 1992). Since our concern is the effect of the background flow on convection, the mechanisms that maintain the background fields are not discussed in detail.

The governing equations for the perturbation are the momentum equation (Navier–Stokes equation), the continuity equation, and the advective–diffusive equation for fluid density. By taking the depth of the channel (D) as the scale of length, the viscous time (D^2/ν) as the scale of time t, and the difference between the background density at the top and the bottom (ΓD) as the scale of density ρ, the non-dimensional form of the governing equations is

$$\frac{\partial \boldsymbol{u}}{\partial t} + (\boldsymbol{u}\cdot\nabla)\boldsymbol{u} + Re\, y\frac{\partial \boldsymbol{u}}{\partial x} + Re\, v\hat{\boldsymbol{i}} + Ta^{1/2}\hat{\boldsymbol{k}}\times\boldsymbol{u} = -\nabla p - Pr^{-1}Ra\,\rho\hat{\boldsymbol{k}} + \nabla^2\boldsymbol{u}, \tag{1}$$

$$\nabla\cdot\boldsymbol{u} = 0, \tag{2}$$

$$\frac{\partial \rho}{\partial t} + \boldsymbol{u}\cdot\nabla\rho + Re\, y\frac{\partial \rho}{\partial x} + w = Pr^{-1}\nabla^2\rho, \tag{3}$$

where $\boldsymbol{u} = (u, v, w)$ is the velocity vector (normalized by ν/D), p is the pressure (normalized by $\rho_0\nu^2/D^2$), and $\hat{\boldsymbol{i}}$ and $\hat{\boldsymbol{k}}$ are unit vectors in the x- and z-directions, respectively. Mathematical operators such as ∇ have the conventional meanings.

The non-dimensional parameters that determine the perturbation growth are

$$\text{Prandtl number:} \quad Pr = \frac{\nu}{\kappa},$$

$$\text{Rayleigh number:} \quad Ra = \frac{g\Gamma D^4}{\rho_0\kappa\nu},$$

$$\text{Reynolds number:} \quad Re = \frac{\Lambda D^2}{\nu},$$

$$\text{Taylor number:} \quad Ta = \frac{4\Omega^2 D^4}{\nu^2},$$

where g is the acceleration due to gravity. For simplicity, Pr is fixed at 1.0. The horizontal lids are assumed to be smooth and perfectly conducting:

$$\partial u/\partial z = \partial v/\partial z = w = \rho = 0 \quad \text{at} \quad z = -1, 0.$$

These boundary conditions are selected to allow the simplest mathematical procedure in the linear analysis (§4). Note that an alteration of the above boundary conditions modifies only the vertical structure of the convection and does not qualitatively change the present results.

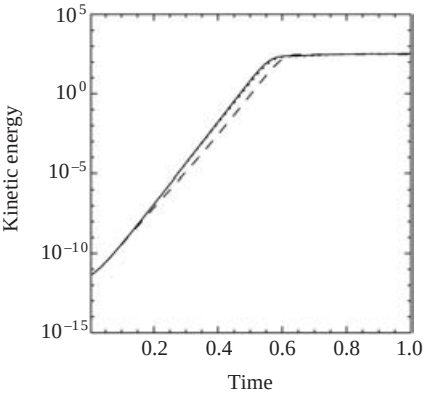

FIGURE 2. Time evolution of KE for $Re = 1$ (solid line), $Re = 2.5$ (dotted line), and $Re = 10$ (dashed line) in the non-rotating case ($Ra = 5.2 \times 10^3$, $Ta = 0$). Semi-logarithmic coordinates are used.

3. Numerical experiments

To examine whether with horizontal shear a transverse roll is preferred to a parallel roll, numerical experiments are initially performed. Since numerical experiments cannot treat infinite regions, non-slip sidewalls are introduced at $y = \pm L/D$ while a periodic condition in the x-direction is assumed for $-L/2D \leqslant x \leqslant L/2D$. In this study, D/L (aspect ratio) is set so small ($\leqslant 0.1$) that the sidewalls have a negligible effect on the linear growth of the perturbation (Davies-Jones 1971). This is confirmed by the experiment with $D/L = 0.05$ which shows no qualitative difference from that with $D/L = 0.1$. The boundary conditions at the sidewalls are

$$u = v = w = \rho = 0 \quad \text{at} \quad y = \pm 10 \ (\pm L/D).$$

Alterations to the above boundary conditions do not qualitatively change the horizontal structure of the convection away from the sidewalls as long as D/L is small.

Equations (1)–(3) are integrated numerically using the SMAC scheme (Amsden & Harlow 1970; Akitomo 1999). The model domain of $10 \times 20 \times 1$ is divided into $128 \times 256 \times 8$ grid boxes and the governing equations are discretized using the finite difference method with a second-order central difference scheme. A grid resolution of $128 \times 256 \times 8$ is sufficient for the present purpose since the experiment with $256 \times 512 \times 16$ grid boxes gives a similar result. Time integration is carried out using the leap-frog scheme together with the Matsuno scheme (Matsuno 1966). Random perturbations of the density ($\rho = 2 \times 10^{-5}$) are initially ($t = 0$) imposed to excite convection.

3.1. *Non-rotating case* ($Ta = 0$)

First, convection in the non-rotating frame of reference ($Ta = 0$) is examined. In this case, Ra is taken to be 5.2×10^3. Without both the horizontal velocity shear ($Re = 0$) and the sidewall, classical linear theory gives the growth rate (referred to as σ^l) and the wavenumber of the most unstable perturbation to be 31.3 and 3.50, respectively.

Figure 2 shows the time evolution of the total kinetic energy (KE) of the perturbation for $Re = 1$, 2.5 and 10. KE increases almost exponentially with time until $t \simeq 0.55$, although a decrease in its growth rate becomes evident as Re increases (e.g. $0.2 \leqslant t \leqslant 0.4$ for $Re = 10$). After $t \simeq 0.55$, KE continues to grow, but its

growth rate become much smaller due to an increasing nonlinear interaction of finite-amplitude perturbation. Figure 3 shows a horizontal section ($-5 \leqslant x, y \leqslant 5$) of the vertical velocity at $t = 0.6$. For $Re = 1$ and 2.5 (figure 3*a*, *b*), cellular (hereafter referred to as C-type) convection appears during the experiment ($0 \leqslant t \leqslant 1.0$) as for $Re = 0$ (not shown), though the convection cell for $Re = 2.5$ seems to be aligned in the transverse direction. For $Re = 10$, on the other hand, C-type convection appears first ($0 \leqslant t \leqslant 0.2$) (not shown), changes into parallel roll (hereafter referred to as P-type) convection, and becomes finite in amplitude (figure 3*c*). This P-type convection continues until the end of the experiment ($t = 1.0$).

The similarities in the convection patterns among $Re = 0$, 1, and 2.5 indicate that the effect of the horizontal velocity shear is negligible for $Re \leqslant 2.5$, although the alignment of cellular convection in the transverse direction for $Re = 2.5$ might suggest a relationship between the horizontal velocity shear and the transverse rolls. On the other hand, the P-type convection observed for $Re = 10$ (figure 3*c*) indicates a strong influence of the horizontal velocity shear on convection. Further experiments for $Re = 5$, 50, and 100 show no qualitative difference from that at $Re = 10$. These results show that when the horizontal velocity shear is large, convection tends to be organized into parallel rolls in the non-rotating case, as concluded by Davies-Jones (1971).

3.2. *Rotating case* ($Ta \neq 0$)

Next, convection in the rotating frame ($Ta \neq 0$) is examined. Since the present concern is whether or not the effect of the horizontal velocity shear on the convection structure is modified by the rotation, and is not the well-known stabilizing effect of the rotation, both Ra and Ta are taken to be 10^4 in order for the linear growth rate without the horizontal shear and sidewalls (σ^l) to have the same value as in the non-rotating case (31.3). The time evolution of KE (not shown) is therefore similar to that in the non-rotating case.

Figure 4 shows a horizontal section of the vertical velocity at $t = 0.6$ for $Re = 1$, 2.5 and 10. C-type convection is observed during the experiment for $Re = 1$ (figure 4*a*) as for $Re = 0$ (not shown). For $Re = 2.5$, the C-type convection also appears until $t \leqslant 0.56$ (not shown). Thereafter, however, transverse roll (hereafter referred to as T-type) convection becomes clearly identified and becomes finite in amplitude (figure 4*b*). T-type convection is sheared by the background flow, so that the angle of the roll axis to the x-direction decreases with time. After $t \simeq 0.72$, T-type convection is broken down into C-type convection (not shown) that continues until the end of the experiment ($t = 1.0$). This breakdown into C-type convection is probably due to the nonlinear effect of the perturbation (described later). For $Re = 10$, on the other hand, C-type convection appears at first ($0 \leqslant t \leqslant 0.12$) (not shown), while P-type convection appears at the end ($t \geqslant 0.32$) and becomes finite in amplitude (figure 4*c*), as in the non-rotating case. Noteworthy is that at the middle stage ($0.12 \leqslant t \leqslant 0.32$), T-type convection is identified as shown in figure 5, though it is not as clear as in figure 4(*b*).

The type of finite-amplitude convection at onset is examined by further experiments for several sets of Ra, Re, and Ta. The results are shown in figure 6. If Ra and Ta are chosen so that σ^l is 31.3 (figure 6*a*), T-type convection appears (though only for a short period of time just after onset) in the rapidly rotating case ($Ta \geqslant 10^4$) when $Re = 2.5$, while it does not appear in the slowly rotating case ($Ta \leqslant 10^2$). On the other hand, in a series of experiments with $Ta = 10^4$ (figure 6*b*), T-type convection appears for smaller (larger) Ra if Re is smaller (larger). The transformation in convection

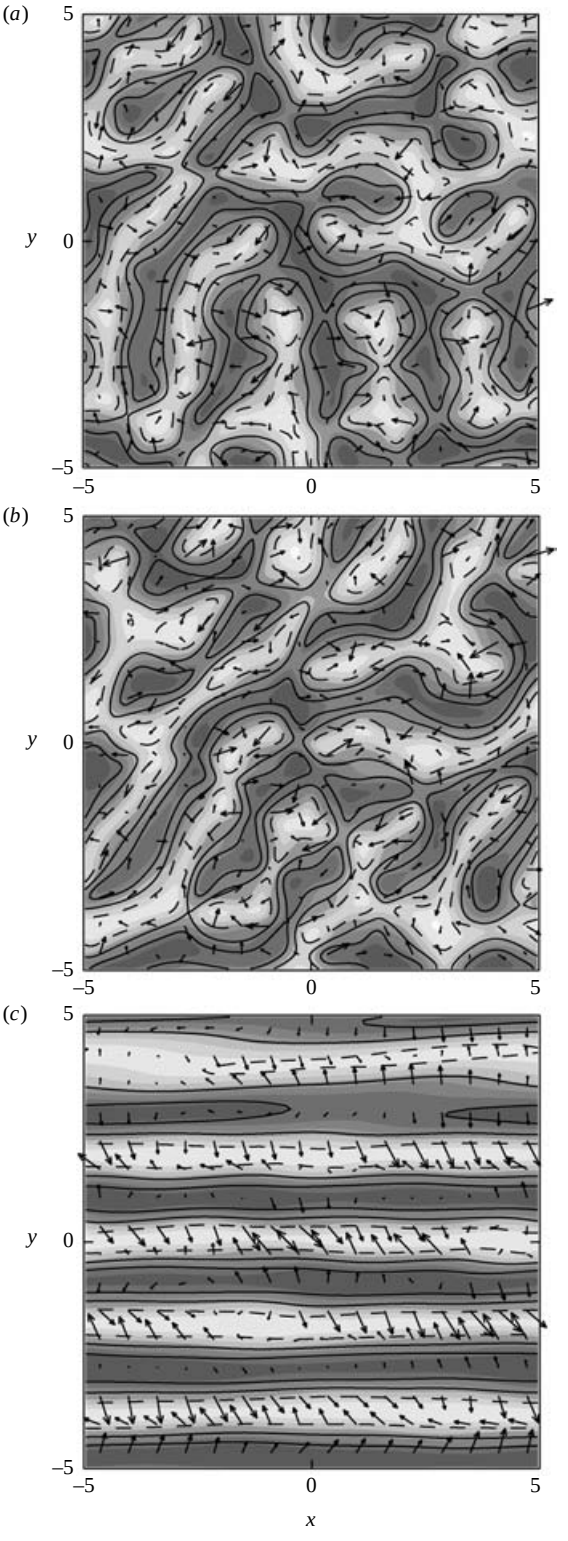

FIGURE 3. Horizontal velocity vectors (arrows), vertical velocity (lines), and density (shading) at $t = 0.6$ in the non-rotating case ($Ra = 5.2 \times 10^3$, $Ta = 0$). Contour (shading) interval for vertical velocity (density) is half (fourth) of its largest value. (*a*) $Re = 1$, (*b*) $Re = 2.5$, and (*c*) $Re = 10$.

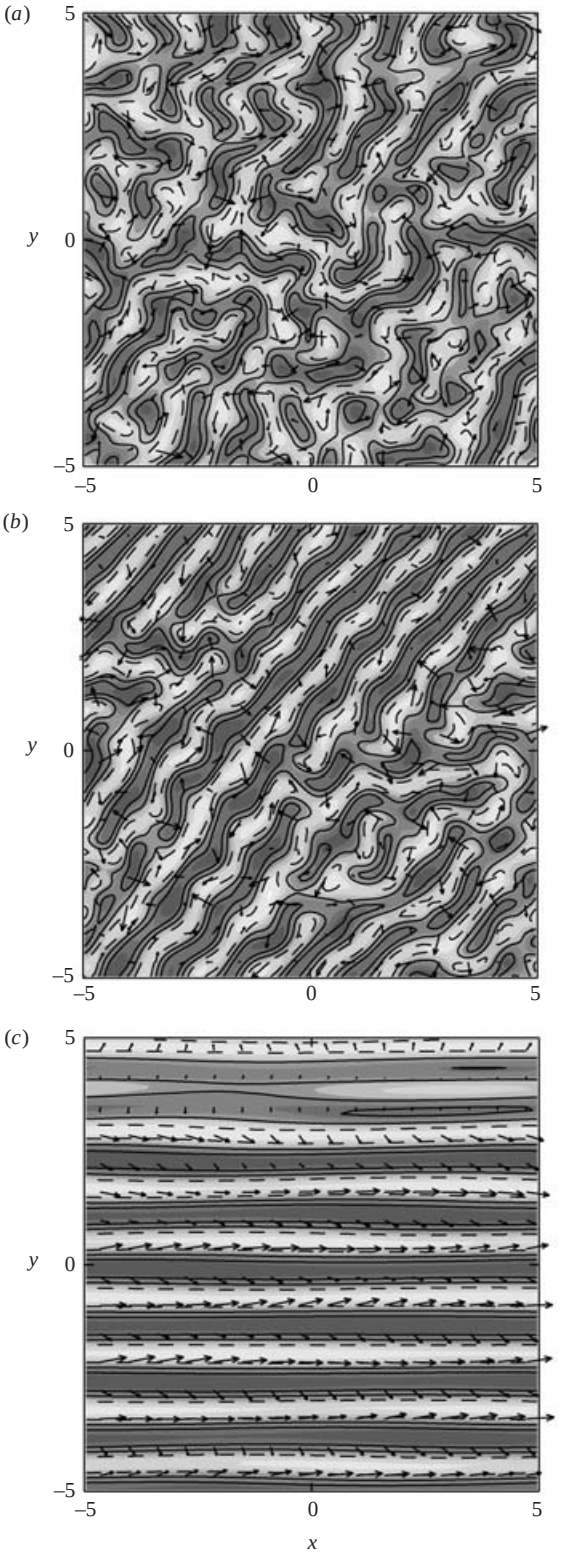

FIGURE 4. As figure 3 but for the rotating case ($Ra = Ta = 10^4$).

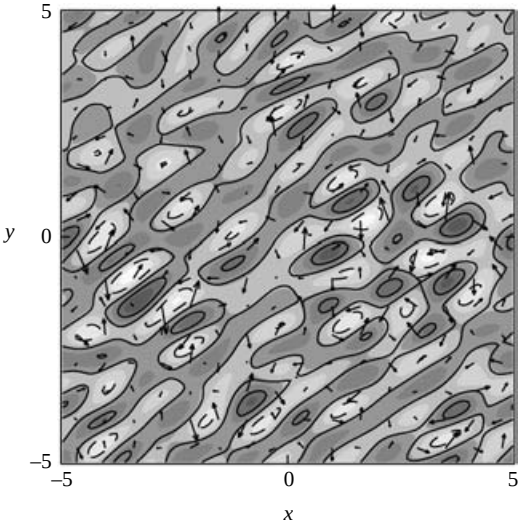

FIGURE 5. As figure 4(*c*) but at $t = 0.16$.

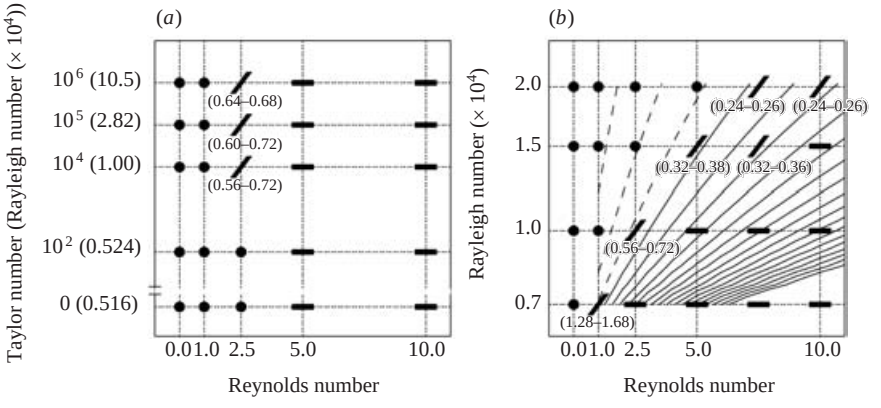

FIGURE 6. (*a*) Type of finite-amplitude convection as a function of *Re* and *Ta*. ●, /, and – represent C-, T-, and P-type convection, respectively. *Ra* is chosen so that σ^l is 31.3. The observed period for T-type convection of finite amplitude is written in brackets below the symbol. In the experiments for $Ta \geqslant 10^5$, a model domain of $5 \times 10 \times 1$ (horizontal extent is half of the original) is used because of the small horizontal scale of convection due to the rapid rotation. (*b*) Type of convection as a function of *Re* and *Ra* ($Ta = 10^4$). Contour lines show T_{fn}/T_{tr}. Contour interval is 0.25. Solid (dashed) lines show $T_{fn}/T_{tr} \geqslant 1 (< 1)$.

type observed in the slowly rotating case ($Ta \leqslant 10^2$) and the rapidly rotating case ($Ta \geqslant 10^4$) is similar to those observed for $Ta = 0$ and $Ta = 10^4$, respectively.

The above results allow us to suggest the following scenario for the determination of the type of finite-amplitude convection at its onset. In the linear stage of perturbation growth, the horizontal velocity shear transforms the horizontal structure of the convection. Although the transformation is from C-type to P-type in the non-rotating or slowly rotating case, it is from C-type to P-type via T-type in the rapidly rotating case. The speed of the transformation increases with the horizontal velocity shear *Re*. (In fact, for $Ta = 10^4$ convection is transformed rapidly into T-type ($t \simeq 0.16$)

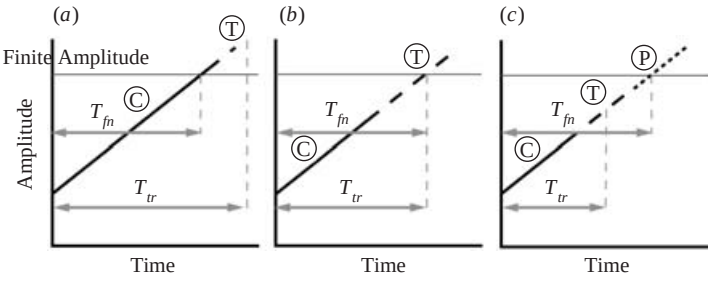

FIGURE 7. Schematic representation of the time evolution of perturbation amplitude (such as figure 2) and time variation of convection type in the rapidly rotating case. Solid, broken, and dotted lines represent C-, T-, and P-type convection, respectively. (*a*) $T_{tr} > T_{fn}$ when Re is small. (*b*) $T_{tr} \simeq T_{fn}$ when Re is intermediate. (*c*) $T_{tr} < T_{fn}$ when Re is large.

and P-type ($t \simeq 0.32$) for $Re = 10$, while it is transformed at a moderate rate into T-type ($t \simeq 0.56$) for $Re = 2.5$.) Thus, the type of finite convection at its onset is the type that exists at the time a perturbation becomes finite in amplitude. As a result, T-type convection can be observed in the rapidly rotating case if the time for the perturbation to become finite in amplitude (T_{fn}) is comparable to the time to transformation into T-type (T_{tr}), as schematically shown in figure 7.

The above scenario is validated by estimating T_{fn} and T_{tr} as follows: T_{fn} is a function of the growth rate (σ), the initial amplitude (A_0) and the finite amplitude (A_f) of the perturbation. If σ is roughly approximated as σ^l (which is constant in time), T_{fn} can be estimated as $(\sigma^l)^{-1}\log(A_f/A_0 + 1)$. On the other hand, T_{tr} should be proportional to Re^{-1} (non-dimensional time scale of the horizontal velocity shear). From the experiments for $Ta \geqslant 10^4$, T_{tr} is estimated as $1.5Re^{-1}$. In figure 6(*a*), σ^l is fixed at 31.3, so that $T_{fn} \simeq 0.6$ in these experiments. As a result, T-type convection appears when $Re = 2.5$ ($T_{tr} \simeq 0.6$) in the rapidly rotating case ($Ta \geqslant 10^4$). In figure 6(*b*), the contour lines of T_{fn}/T_{tr} are also superimposed. This clearly shows that in the rapidly rotating case, T-type convection appears when $T_{fn} \simeq T_{tr}$, while C-type (P-type) convection is found when $T_{fn} < T_{tr}$ ($T_{fn} > T_{tr}$).

Note that after the nonlinear effect of the finite-amplitude perturbation becomes significant, the above scenario is no longer valid. The nonlinear effect does not change the horizontal structure of C- and P-type convection, but it changes T-type into C-type convection. One reason for this change is as follows: The background flow shears the horizontal pattern of convection and tends to align convection into the x-direction. However, once the transverse roll becomes of finite amplitude, the perturbation itself continues to generate variations in velocity and density in the original transverse direction, regardless of the shearing of the background flow. As a result, there exist two preferred orientations, and hence the convection roll is likely to be broken down into small cells (C-type). The other reason may be the sidewall which affects the interior region in the nonlinear stage. In the rotating case, convection near the sidewall has different properties (such as the wavenumber and the growth rate) from that in the interior. This is because the fluid near the wall can escape from the constraint of the Coriolis acceleration. (This situation is the same as that for Kelvin waves, which is that the gravity wave near the wall can escape from the Coriolis constraint and hence escape from being an inertial gravity wave.) In the linear stage, this effect is localized near the wall. However, in the later nonlinear stage, the effect is gradually advected into the interior to contaminate convection there. This is probably

one of the reasons why the re-formation of the convection roll in the rotating frame (Kuppers & Lortz 1969) is hardly observed in the present experiment.

4. Linear analysis

In the previous section, we found that T-type convection is formed in the rapidly rotating frame as long as $T_{fn} \simeq T_{tr}$. The next question is therefore why the transformation into the T-type occurs only in the rapidly rotating frame, which is investigated in this section by linear analysis.

4.1. *Formulation of the problem*

The basic equations are the linearized version of (1)–(3). The y-component of $\nabla \times (1)$ (vorticity equation), the y-component of $\nabla \times \nabla \times (1)$, and ∇_z^2 (3) ($\nabla_z^2 = \partial^2/\partial x^2 + \partial^2/\partial z^2$) constitute the reduced set of governing equations for $\eta (= \partial u/\partial z - \partial w/\partial x)$ (the y-component of vorticity), v, and ρ as

$$\left(\frac{\partial}{\partial t} + Re\, y\frac{\partial}{\partial x}\right)\eta - \left(Ta^{1/2} - Re\right)\frac{\partial v}{\partial z} = Pr^{-1}Ra\frac{\partial \rho}{\partial x} + \nabla^2\eta, \tag{4}$$

$$\left(\frac{\partial}{\partial t} + Re\, y\frac{\partial}{\partial x}\right)\nabla^2 v + Ta^{1/2}\frac{\partial \eta}{\partial z} = Pr^{-1}Ra\frac{\partial^2 \rho}{\partial y \partial z} + \nabla^4 v, \tag{5}$$

$$\left(\frac{\partial}{\partial t} + Re\, y\frac{\partial}{\partial x}\right)\nabla_z^2\rho - \left(\frac{\partial \eta}{\partial x} + \frac{\partial^2 v}{\partial y \partial z}\right) = Pr^{-1}\nabla^2\nabla_z^2\rho. \tag{6}$$

From (2), u and w are expressed using η and v as

$$\nabla_z^2 u = \frac{\partial \eta}{\partial z} - \frac{\partial^2 v}{\partial x \partial y}, \quad \nabla_z^2 w = -\frac{\partial \eta}{\partial x} - \frac{\partial^2 v}{\partial y \partial z}. \tag{7}$$

In Davies-Jones (1971), the growth rate of the perturbation is assumed to be constant in time. However, such a solution cannot represent the transformation from C- to P- via T-type convection. In fact, the growth rate of KE observed in the numerical experiments is not constant even in the linear stage (figure 2), which demonstrates the invalidity of such an assumption. One way to examine such transient linear dynamics may be the optimal perturbation method (Farrell 1993). In order to apply this method to the present problem, however, the sidewall should be introduced as in the numerical experiment. Although such an analysis is useful for understanding the results of numerical experiments, the effect of horizontal velocity shear itself is not illustrated clearly due to the effect of the sidewall (which is not at present of concern). The exclusion of the sidewall is particularly important when transverse rolls in the atmosphere and oceans are considered.

Instead of assuming a constant growth rate or a sidewall, we assume that the horizontal structure of the perturbation is sheared by the background flow $\overline{u} = Re\, y$, as observed in the numerical experiments. Thus, we take solutions of the form

$$\left.\begin{aligned} \eta(x, y, z, t) &= H_{kl}(t)\exp \mathrm{i}(k(x - Re\, yt) + ly)\sin(\pi z), \\ v(x, y, z, t) &= V_{kl}(t)\exp \mathrm{i}(k(x - Re\, yt) + ly)\cos(\pi z), \\ \rho(x, y, z, t) &= P_{kl}(t)\exp \mathrm{i}(k(x - Re\, yt) + ly + \pi/2)\sin(\pi z), \end{aligned}\right\} \tag{8}$$

where $H_{kl}(t)$, $V_{kl}(t)$, and $P_{kl}(t)$ are time-dependent amplitudes of η, v, and ρ, respectively. In this study, the above form of the solution is referred to as the Lagrangian mode. Note that the actual wavenumber in the y-direction is given by

$l - kRe\,t(=\tilde{l}(t))$, which varies in time if $kRe \neq 0$. Without loss of generality, $k \geqslant 0$ is taken. P-type convection is represented by the Lagrangian mode $k = 0$, while T-type is represented by $k > 0$. Hereafter, the mode $k = 0$ is called the P-mode, while the mode $k > 0$ is called the T-mode.

Note that the above form of the solutions can be applied to the infinite horizontal layer bounded at the top and the bottom lids (figure 1), so that only the effect of the horizontal velocity shear on convection can be examined. In this configuration, the boundary condition is written as

$$\partial v/\partial z = \eta = \rho = 0 \quad \text{at} \quad z = 0, -1,$$

which is satisfied by (8).

Transforming the partial differential operator in (4)–(6) as

$$\frac{\partial}{\partial t} \to \frac{\mathrm{d}}{\mathrm{d}t} - \mathrm{i}kRe\,y,$$
$$\frac{\partial}{\partial x} \to \mathrm{i}k,$$
$$\frac{\partial}{\partial y} \to \mathrm{i}\tilde{l}(t),$$
$$\frac{\partial}{\partial z} \to \pi \text{ or } -\pi,$$
$$\nabla^2 \to -k^2 - \tilde{l}(t) - \pi^2 \equiv -a_{kl}(t)^2 - \pi^2,$$
$$\nabla_z^2 \to -k^2 - \pi^2 \equiv -b^2,$$

the substitution of (8) into (4)–(6) results in the following ordinary differential equations with respect to time for $H_{kl}(t)$, $V_{kl}(t)$, and $P_{kl}(t)$:

$$\frac{\mathrm{d}}{\mathrm{d}t}H_{kl}(t) + \pi\left(Ta^{1/2} - Re\right)V_{kl}(t) = -kPr^{-1}RaP_{kl}(t) - (a_{kl}(t)^2 + \pi^2)H_{kl}(t),$$
$$\frac{\mathrm{d}}{\mathrm{d}t}(-a_{kl}(t)^2 - \pi^2)V_{kl}(t) + \pi Ta^{1/2}H_{kl} = -\pi\tilde{l}(t)Pr^{-1}RaP_{kl}(t) - (a_{kl}(t)^2 + \pi^2)^2V_{kl}(t),$$
$$\frac{\mathrm{d}}{\mathrm{d}t}(-b^2)P_{kl}(t) - kH_{kl}(t) + \pi\tilde{l}(t)V_{kl}(t) = -b^2\left(-a_{kl}^2 - \pi^2\right)^2Pr^{-1}P_{kl}(t).$$

Noting that $\mathrm{d}(a_{kl}(t)^2)/\mathrm{d}t = -2k\tilde{l}(t)Re$, further manipulation yields

$$\frac{\mathrm{d}}{\mathrm{d}t}\begin{pmatrix} H_{kl}(t) \\ V_{kl}(t) \\ P_{kl}(t) \end{pmatrix} = \boldsymbol{A}_{kl}(t)\begin{pmatrix} H_{kl}(t) \\ V_{kl}(t) \\ P_{kl}(t) \end{pmatrix}, \tag{9}$$

$$\boldsymbol{A}_{kl}(t) = \begin{pmatrix} -(a_{kl}(t)^2 + \pi^2) & -\pi\left(Ta^{1/2} - Re\right) & -kPr^{-1}Ra \\ \dfrac{\pi}{a_{kl}(t)^2 + \pi^2}Ta^{1/2} & \dfrac{2k\tilde{l}(t)}{a_{kl}(t)^2 + \pi^2}Re - (a_{kl}(t)^2 + \pi^2) & \dfrac{\pi\tilde{l}(t)}{a_{kl}(t)^2 + \pi^2}Pr^{-1}Ra \\ -\dfrac{k}{b^2} & \dfrac{\pi\tilde{l}(t)}{b^2} & -(a_{kl}(t)^2 + \pi^2)Pr^{-1} \end{pmatrix}. \tag{10}$$

Two effects of the horizontal velocity shear appear in $\boldsymbol{A}_{kl}(t)$. One is the acceleration (or deceleration) of u by the interplay of the horizontal velocity shear and v (the

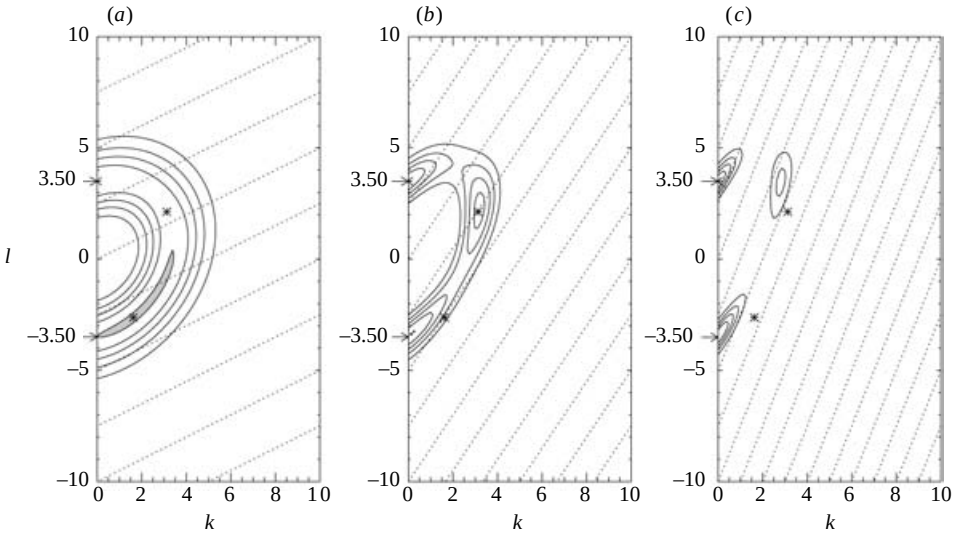

FIGURE 8. $P_{kl}(t)$ for $Re = 2.5$ in the non-rotating case ($Ra = 5.2 \times 10^3$, $Ta = 0$). (*a*) $t = 0.2$ ($P_{max} = 5.37 \times 10^2$), (*b*) $t = 0.6$ ($P_{max} = 1.46 \times 10^8$), and (*c*) $t = 1.0$ ($P_{max} = 1.01 \times 10^{13}$). Contour interval is one fifth of the largest $P_{kl}(t)$ of P-mode ($k = 0$). Shading represents larger $P_{kl}(t)$ of the T-mode ($k > 0$) than the largest $P_{kl}(t)$ of the P-mode ($k = 0$). Dotted lines show the isolines of $\tilde{l}(t)$. Asterisks mark points $(k, l) = (0, 3.50)$, $(1.63, -2.63)$, and $(3.13, 2.13)$.

term $Re\, v\hat{\boldsymbol{i}}$ in (1)), which is given by πRe from the term $-\pi(Ta^{1/2} - Re)$ in $\boldsymbol{A}_{kl}(t)$. We refer to this effect as the Reynolds acceleration. The other is the time variation of $a_{kl}(t)$, expressed by the elements that include $a_{kl}(t)^2$. Note that if $\boldsymbol{A}_{kl}(t)$ is considered at a fixed time, this effect is expressed only by the term $2k\tilde{l}(t)Re/(a_{kl}(t)^2 + \pi^2)$, which originates from $\mathrm{d}(a_{kl}(t)^2)/\mathrm{d}t$. This effect is understood clearly if neutrally stratified ($Ra = 0$) inviscid fluid in the non-rotating frame ($Ta = 0$) is considered. In such a situation, (9) is easily solved to obtain $V_{kl}(t) = V_0/(a_{kl}(t)^2 + \pi^2)$ where V_0 is constant. Thus, the time variation in $a_{kl}(t)$ causes the time variation of $V_{kl}(t)$ (and others) so as to conserve $(a_{kl}(t)^2 + \pi^2)|V_{kl}(t)|$. These two effects are important for the instantaneous growth of the each Lagrangian mode, as described later.

4.2. *Time evolution of the perturbation amplitude*

The time integration of (9) is carried out numerically using the Adams scheme. The values of k and l are varied from 0 to 10 and -10 to 10, respectively, at an interval of 0.125. The most unstable eigenvector of $\boldsymbol{A}_{kl}(0)$ is used for $H_{kl}(0)$, $V_{kl}(0)$, $P_{kl}(0)$. $P_{kl}(t)$ is used to determine the preferred mode. A much larger $P_{kl}(t)$ for $k > 0$ (T-mode) than for $k = 0$ (P-mode) corresponds to the T-type convection observed in the numerical experiments, while a much smaller $P_{kl}(t)$ for $k > 0$ than that for $k = 0$ corresponds to P-type convection. Otherwise, C-type convection appears.

4.2.1. *Non-rotating case* ($Ra = 5.2 \times 10^3$, $Ta = 0$)

Figure 8 shows $P_{kl}(t)$ at $t = 0.2, 0.6$ and 1.0 for $Re = 2.5$ as a function of k and l. Although for $Re = 0$ $P_{kl}(t)$ is largest on the semicircle $a_{kl} = 3.50$ at all times (not shown), for $Re = 2.5$ $P_{kl}(t)$ is gradually distorted with time from a semicircular to a heterogeneous distribution. At $t = 0.2$ (figure 8*a*), $P_{kl}(t)$ is largest at $(k, l) = (1.63, -2.63)$ (T-mode), which is slightly (2.22%) larger than that at $(k, l) = (0, \pm 3.50)$ (P-mode). However, the general pattern of $P_{kl}(t)$ is still similar to that for $Re = 0$.

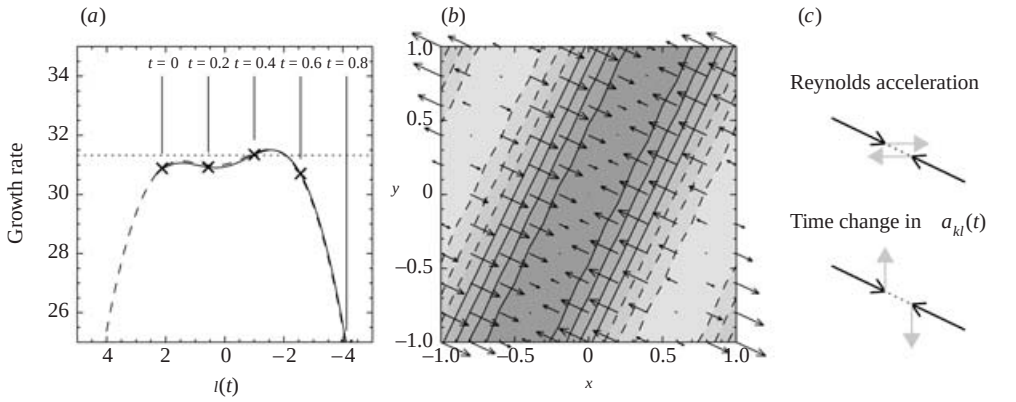

FIGURE 9. (*a*) Time evolution of $\sigma_T(t)$ of the Lagrangian mode $(k, l) = (3.13, 2.13)$ in the non-rotating case ($Ra = 5.2 \times 10^3$, $Ta = 0$). Time is labelled near the top of the figure. The horizontal axis is $\tilde{l}(t)$. The corresponding σ_T^e is also plotted as a dashed line. Dotted line represents $\sigma_P(t)$. (*b*) Horizontal velocity vectors, vertical velocity (lines), and density (shading) of the most unstable eigenmode at $\tilde{l}(t) = -1.50$. Solid (dashed) line represents downward (upward) velocity, while the dark (light) shading represents positive (negative) density. (*c*) Schematics of the horizontal velocity vector (black arrows) and the velocity change due to the Reynolds acceleration (grey solid arrows in the upper panel) and the velocity change due to the time variation in a_{kl} (grey solid arrows in the lower panel). The direction normal to the roll axis is denoted by the dotted line.

At $t = 0.6$ (figure 8*b*), larger values remain only at around $(k, l) = (3.13, 2.13)$ (T-mode) and $(k, l) = (0, \pm 3.50)$ (P-mode). The former is 12.3% smaller than the latter. At $t = 1.0$ (figure 8*c*), only the $P_{kl}(t)$ of the P-mode at around $(k, l) = (0, \pm 3.50)$ continues to grow and the $P_{kl}(t)$ of the T-mode at $k > 0$ becomes much smaller.

The above time evolution of $P_{kl}(t)$ for $Re = 2.5$ is consistent with the scenario suggested in § 3. That is, the perturbation grows linearly while transforming its horizontal structure from C-type (figure 8*a*, *b*) to P-type (figure 8*c*) in the non-rotating case. In the numerical experiment for $Re = 2.5$, the perturbation becomes finite in amplitude at $t \simeq 0.6$ (figure 8*b*), so that C-type convection is observed (figure 3*b*). Note that the nonlinear effect becomes significant thereafter in the numerical experiment and hence C-type convection continues until the end of the experiment ($t = 1.0$). The relatively larger $P_{kl}(t)$ at $(k, l) = (3.13, 2.13)$ at $t = 0.6$ (figure 8*b*) contributes to a transverse alignment of the C-type convection (figure 3*b*). In fact, the spectrum of density perturbations in the numerical experiment (not shown) shows larger peaks at $(k, l) \simeq (3.1, 2.2)$ and $(0, 3.1)$ in the wavenumber space (the former being smaller than the latter). It should also be noted that the transition from the semicircular distribution of $P_{kl}(t)$ to a heterogeneous one becomes faster with increasing Re (not shown), which corresponds to the faster transformation from C-type to P-type observed in the numerical experiment.

Figure 9 shows the time evolution of the growth rate of $P_{kl}(t)$ for $(k, l) = (3.13, 2.13)$ (referred to as $\sigma_T(t)$). The horizontal axis is $\tilde{l}(t) (= l - k\,Re\,t)$. The dotted line shows the growth rate of $(k, l) = (0, \pm 3.50)$ (referred to as $\sigma_P(t)$), which is constant in time. Noteworthy is that $\sigma_T(t)$ is slightly larger than $\sigma_P(t)$ at $0.39 \leqslant t \leqslant 0.53$. Thus, even in the non-rotating case, the T-mode can grow faster than the P-mode. However, $\sigma_T(t)$ at the other times is much smaller than $\sigma_P(t)$ so that $P_{kl}(t)$ of the T-mode could never be larger than that of the P-mode in the non-rotating case.

Although the net effect of the horizontal velocity shear on the T-mode is thus small, it would be instructive to know why $\sigma_T(t)$ can be larger than $\sigma_P(t)$. To this end, the eigenmode of $\boldsymbol{A}_{kl}(t)$ with the largest eigenvalue is investigated. This eigenmode represents the most preferred mode by the background field 'at fixed time t'. Therefore, it mirrors the 'instantaneous' dynamics of the background field in which the effects of the Reynolds acceleration and the time change in $a_{kl}(t)$ at that instant are included. On the other hand, the Lagrangian mode reflects 'integrated' dynamics 'until that time'. Eigen analysis is thus useful for identifying each effect of the background field at each time, one by one. Since the eigenmode changes with time if $kRe \neq 0$, the Lagrangian mode generally differs from the eigenmode, even though they are the same at $t = 0$.

The dashed line in figure 9(a) shows the largest eigenvalue of $(k, l) = (3.13, 2.13)$ (referred to as σ_T^e). Note that the largest eigenvalue of the P-mode is the same as $\sigma_P(t)$. Although $\sigma_T(t)$ is slightly smaller than σ_T^e, the time variation of $\sigma_T(t)$ is explained well by that of σ_T^e. Two peaks of σ_T^e are found at around $\tilde{l}(t) = \pm 1.5$ at which $a_{kl}(t)$ becomes close to the most preferred value (3.50) for perturbation growth with the present Ra and Ta. The difference in σ_T^e at the two peaks is due to the effects of Reynolds acceleration and the time change in $a_{kl}(t)$. Figures 9(b) and 9(c) show the perturbation structure and a schematic representation of the above two effects at $\tilde{l}(t) = -1.50$. The Reynolds acceleration acts to increase $|u|$, as represented by the grey arrows in the upper panel of figure 9(c). On the other hand, the time change in $a_{kl}(t)$, represented by the grey arrows in the lower panel acts to decrease $|v|$. The comparison of the eigenmode of $\boldsymbol{A}_{kl}(t)$ without the effect of the Reynolds acceleration (the term πRe) and that without the effect of the time variation of $a_{kl}(t)$ (the term $2k\tilde{l}(t)Re/(a_{kl}(t)^2 + \pi^2)$) makes it clear that the former effect is larger than the latter. As a result, convergence of the velocity component normal to the roll axis is increased. By virtue of the continuity of fluid (equation (2)), increased convergence enhances the vertical velocity and thus the conversion of potential energy, so that the growth rate increases. At $\tilde{l}(t) = 1.50$, the situation is reversed, and hence potential energy conversion and the growth rate at that time are decreased by the horizontal velocity shear.

4.2.2. *Rotating case* ($Ra = Ta = 10^4$)

Figure 10 shows $P_{kl}(t)$ for $Re = 2.5$ at $t = 0.2$, 0.6 and 1.0. At $t = 0.2$ (figure 10a), $P_{kl}(t)$ is slightly distorted from a semicircular distribution. Though $P_{kl}(t)$ for around $(k, l) \simeq (5.13, 1.50)$ (T-mode) is slightly (8.06%) larger than that for $(k, l) = (0, \pm 5.25)$ (P-mode), the general pattern of $P_{kl}(t)$ differs little from that for $Re = 0$, as in the non-rotating case. By $t = 0.6$ (figure 10b), on the other hand, $P_{kl}(t)$ for $(k, l) = (4.75, 3.63)$ becomes much (20.1%) larger than that for $(k, l) = (0, \pm 5.25)$, in marked contrast to the non-rotating case. At $t = 1.0$ (figure 10c), only $P_{kl}(t)$ for around $(k, l) = (0, \pm 5.25)$ continues to grow, which is again similar to the non-rotating case.

The above time evolution of $P_{kl}(t)$ is also consistent with the scenario suggested in § 3. The transformation from C-type (figure 10a) to P-type (figure 10c) via T-type (figure 10b) convection occurs during the linear growth of a perturbation. In the numerical experiment for $Re = 2.5$, the perturbation becomes finite in amplitude at $t \simeq 0.6$ (figure 10b), so that T-type convection is observed (figure 4b). In fact, the spectrum of density perturbations shows a larger peak at $(k, l) \simeq (4.70, 3.5)$ than at (0, 5.0) in the wavenumber space (not shown).

Figure 11(a) shows the time evolutions of the growth rate of $(k, l) = (4.75, 3.63)$ ($\sigma_T(t)$). The corresponding largest eigenvalue (σ_T^e) is also plotted as a dashed line. The

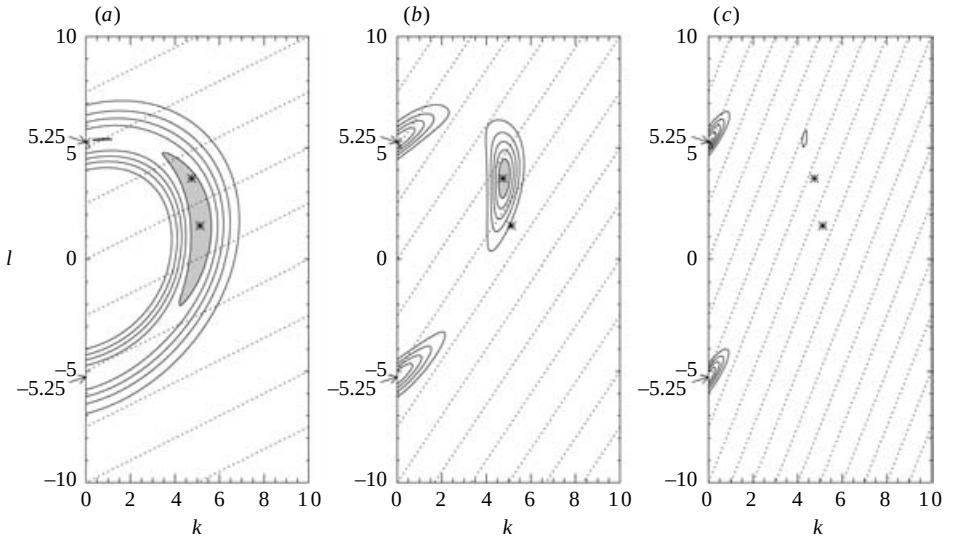

FIGURE 10. As figure 8 but for the rotating case ($Ra = Ta = 10^4$). (*a*) $t = 0.2$ ($P_{max} = 6.80 \times 10^2$). (*b*) $t = 0.6$ ($P_{max} = 2.32 \times 10^8$). (*c*) $t = 1.0$ ($P_{max} = 6.44 \times 10^{13}$). Asterisks mark-points $(k, l) = (0, 5.25)$, (5.13, 1.50) and (4.75, 3.63).

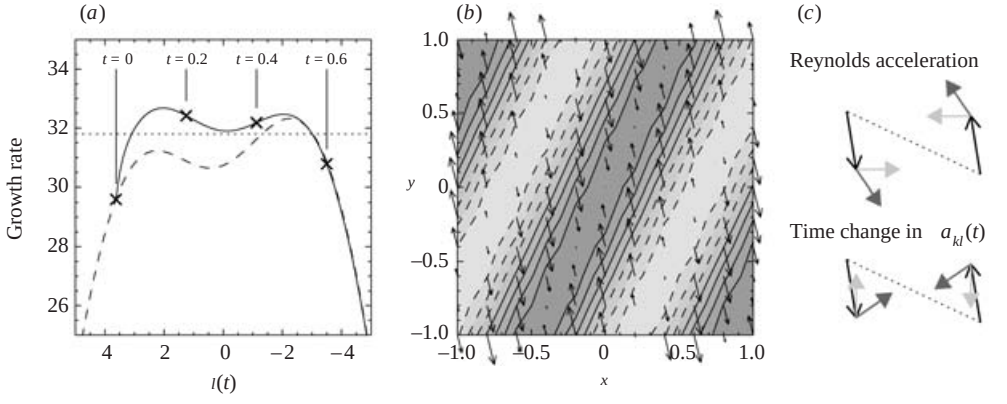

FIGURE 11. As figure 9 but for the rotating case ($Ra = Ta = 10^4$). $(k, l) = (4.75, 3.63)$. Dark grey arrows in (*c*) show the velocity change due to the Reynolds acceleration and the velocity change due to the time variation in a_{kl} subject to the Coriolis acceleration. Light grey arrows represent the velocity changes before the Coriolis acceleration rotates them to the right.

mechanism that makes σ_T^e larger than the growth rate of the P-mode ($\sigma_P(t)$) is similar to the non-rotating case, but is affected by the rotation. At $\tilde{l}(t) = -2.25$ when σ_T^e is largest, the Reynolds acceleration subject to the Coriolis acceleration acts to enhance the convergence of the velocity component normal to the roll axis (figure 11*b*, *c*). Contrary to the non-rotating case (figure 9), the time change in $a_{kl}(t)$ also acts to (though slightly) enhance it. As a result, potential energy conversion is increased to make $\sigma_T^e(t)$ larger than $\sigma_P(t)$. At $\tilde{l}(t) = 2.25$, the situation is reversed, and $\sigma_T^e(t)$ is smaller than $\sigma_P(t)$.

More noteworthy in the rotating case is that $\sigma_T(t)$ is much larger than σ_T^e in the early stage ($t < 0.5$). It is this difference that makes $P_{kl}(t) (= \exp(\int_0^t \sigma_{kl}(t')\,\mathrm{d}t'))$

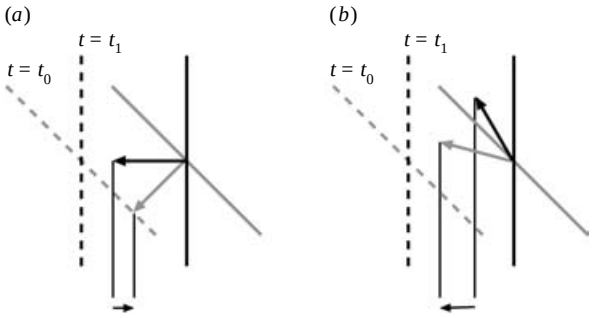

FIGURE 12. Schematic relation between the time evolutions of the Lagrangian mode and eigenmode. (*a*) Non-rotating case, and (*b*) rotating case. Solid (dashed) line shows the line of upward (downward) velocity and large arrows represent the horizontal velocity vector at the top lid. Grey represents the eigenmode at $t = t_0$, while black represents that at $t = t_1 (> t_0)$. Even though the Lagrangian mode is equal to the eigenmode at $t = t_0$, the former deviates from the latter at $t = t_1$. The small arrow represents the difference in the horizontal velocity vector between the Lagrangian mode and eigenmode at $t = t_1$, on the assumption that the Lagrangian mode does not change from $t = t_0$, for simplicity.

of the T-mode much larger than that of the P-mode (figure 10*b*) and hence T-type convection is observable (figure 4*b*) in the rotating case. This difference is explained schematically in figure 12. The axis of the convection roll rotates with time due to shearing of the background flow, and the corresponding horizontal velocity vector of the most unstable eigenmode rotates accordingly. However, the actual horizontal velocity vector of the Lagrangian mode cannot adjust to such rotation completely. This results in the difference between the Lagrangian mode and the corresponding eigenmode. This process occurs in both the non-rotating and rotating cases. In the non-rotating case (figure 12*a*), such an incomplete adjustment slightly reduces the convergence of the horizontal velocity and hence the vertical velocity compared with those of the eigenmode. As a result, $\sigma_T(t)$ is slightly smaller than σ_T^e (figure 9*a*). In the rotating case (figure 12*b*), however, an incomplete adjustment considerably enhances the vertical velocity and the conversion of potential energy. As a result, $\sigma_T(t)$ becomes significantly larger than σ_T^e (figure 11*a*), so that T-type convection appears.

5. Summary

The structure of thermal convection in horizontal plane Couette flow is investigated. Numerical experiments show that the transformation of the horizontal structure takes place in the linear stage of perturbation growth. In a non-rotating or slowly rotating frame of reference, the transformation from cellular (C-type) to parallel roll (P-type) convection occurs. In a rapidly rotating frame of reference, on the other hand, transformation from C-type to P-type via transverse roll (T-type) convection takes place. The speed of the transformation increases with increasing horizontal velocity shear. Therefore, T-type convection of finite amplitude appears if the time for perturbation to finite amplitude is comparable to the time to transformation into T-type. In the later nonlinear stage, T-type convection is broken down into C-type convection, probably due to the nonlinear effect of the finite-amplitude perturbation. Although T-type convection of finite amplitude is thus observed only for a short period of time just after the onset of convection in the rapidly rotating case, this

result reveals a new aspect of the effects of the horizontal shear of the background flow on convection.

The formation mechanism of T-type convection in the linear stage of perturbation growth is investigated by linear analysis. We formulated the problem so that the horizontal structure of the perturbation is sheared by the background flow. This formulation significantly illuminates the underlying dynamics of the perturbation growth in the case where the advection speed of the perturbation is equal to the background flow, as in the present study. By this formulation, the perturbation is separated into the transverse mode (that is sheared by the background flow) and the parallel mode, and the governing equations change from partial to ordinary differential equations for perturbation amplitude with respect to time.

Integration of the ordinary differential equations and a complementary eigen analysis make it clear that the Reynolds acceleration and time change in the total wavenumber of the perturbation can temporarily accelerate the growth of the transverse mode in both the non-rotating and rotating cases. However, their net effects are so small that the transverse mode cannot be much larger than the parallel mode in the non-rotating or slowly rotating case. On the other hand, in the rapidly rotating case where the Coriolis acceleration changes the direction of the horizontal velocity vector significantly to the right, the shearing of the perturbation by the background flow results in enhanced potential energy conversion of the transverse mode. As a result, the transverse mode dominates over the parallel mode.

The present results successfully explain the transverse roll convection simulated by Yoshikawa *et al.* (2001) in which $Ta \sim 10^4$ ($2\Omega = 10^{-4}\,\mathrm{s}^{-1}$, $D \sim 150\,\mathrm{m}$, $\nu = 0.02\,\mathrm{m}^2\,\mathrm{s}^{-1}$), though the actual formation of such transverse rolls remains controversial, since the value of ν in regions of active oceanic convection is unknown. The present result might also explain some aspects of transverse roll convection observed in the atmosphere of planets such as Jupiter whose rotation speed is faster (the rotation period is about 10 hours). In fact, transverse roll convection is observed where the horizontal velocity shear is large, though the tilted rotation vector might also play some role in forming transverse roll convection (e.g. Hathaway & Sommerville 1987). Further identification of the mechanisms relevant to the generation of transverse roll convection in the Jovian atmosphere requires observations of the vertical extent of convection D and eddy viscosity ν. In the atmosphere of the Earth, the vertical extent of cloud streets is so small ($\sim 2\,\mathrm{km}$; Etling & Brown 1993) that Ta is only $\sim$ 200 for $2\Omega \sim 10^{-4}\,\mathrm{s}^{-1}$ (40°N) and $\nu \sim 30\,\mathrm{m}^2\,\mathrm{s}^{-1}$ (Krishnamurti 1975). Thus, the cloud streets are less likely to be organized in the transverse direction by the horizontal velocity shear.

The authors would like to thank Professor A. Masuda of Kyushu University for his helpful advice on eigen analysis. The numerical calculation was done on a VPP5000 at the Computing and Communications Center of Kyushu University. SSL II (Scientific Subroutine Library II) was used for the time integration and eigen analysis in section 4.

REFERENCES

Akitomo, K. 1999 Open-ocean deep convection due to thermobaricity, 2, Numerical experiments. *J. Geophys. Res.* **104**, 5235–5249.

Amsden, A. A. & Harlow, F. H. 1970 The SMAC method: A numerical technique for calculating incompressible fluid flows. LA-4370.

Asai, T. 1970 Three dimensional features of thermal convection in a pale Couette flow. *J. Met. Soc. Japan* **48**, 18–129.

Davies-Jones, R. 1971 Thermal convection in a horizontal plane Couette flow. *J. Fluid Mech.* **49**, 193–205.

Etling, D. & Brown, R. A. 1993 Roll vortices in the planetary boundary layer: A review. *Boundary-Layer Met.* **65**, 215–248.

Farrell, B. F. 1993 Transient development of perturbations in stratified flow. *J. Atmos. Sci.* **50**, 2201–2214.

Hathaway, R. C. & Sommerville, J. 1987 Thermal convection in a rotating shear flow. *J. Fluid Mech.* **38**, 43–68.

Krishnamurti, R. 1975 On cellular cloud patterns. Part 3: Applicability of the mathematical and laboratory models. *J. Atmos. Sci.* **32**, 1373–1383.

Kuettner, J. 1959 The band structure of the atmosphere, *Tellus* **11**, 267–294.

Kuo, H. L. 1963 Perturbations of plane Couette flow in stratified fluid and origin of cloud streets. *Phys. Fluids* **6**, 195–211.

Kuppers, G. & Lortz, D. 1969 Transition from laminar convection to thermal turbulence in a rotating fluid layer. *J. Fluid Mech.* **35**, 609–620.

Matsuno, T. 1966 Numerical integration of the primitive equations by a simulated backward difference method. *J. Met. Soc. Japan* **44**, 187–196.

Miura, Y. 1986 Aspect ratios of longitudinal rolls and convection cells observed during cold air outbreaks. *J. Atmos. Phys.* **43**, 26–39.

Tillmark, N. & Alfredsson, P. H. 1992 Experiments on transition in plane Couette flow. *J. Fluid Mech.* **235**, 89–102.

Yoshikawa, Y., Akitomo, K. & Awaji, T. 2001 Formation process of intermediate water in baroclinic current under cooling. *J. Geophys. Res.* **106**, 1033–1052.